Journal of Power Sources 262 (2014) 72–78

Contents lists available at ScienceDirect

Journal of Power Sources

journal homepage: www.elsevier.com/locate/jpowsour

Template-free synthesis of homogeneous yolk–shell TiO_2 hierarchical microspheres for high performance lithium ion batteries

Xiaobing Wang [a], Yuanyuan Wang [a], Lin Yang [a,b,*], Kui Wang [a,b], Xiangdong Lou [a], Bibo Cai [c]

[a] School of Chemistry and Chemical Engineering, Key Laboratory of Green Chemical Media and Reactions, Ministry of Education, Henan Normal University, Xinxiang 453007, P. R. China
[b] Collaborative Innovation Center of Henan Province for Green Manufacturing of Fine Chemicals, Henan Province, Xinxiang 453007, P. R. China
[c] Xinxiang Tianli Energy Co., Ltd, Henan Province, Xinxiang 453000, P. R. China

HIGHLIGHTS

- The yolk–shell TiO_2 microspheres were synthesized by a template-free method.
- The hierarchical yolk–shell structure ensures the high capacity and cycle stability.
- The prepared TiO_2 delivers a reversible capacity of 191 mAh g^{-1} after 40 cycles.

GRAPHICAL ABSTRACT

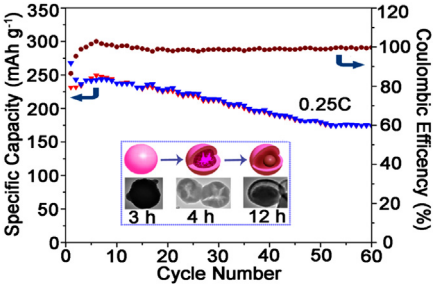

ARTICLE INFO

Article history:
Received 17 November 2013
Received in revised form
19 February 2014
Accepted 19 March 2014
Available online 28 March 2014

Keywords:
Synthesis
Template-free
Yolk–shell
Electrochemical performance

ABSTRACT

The homogeneous yolk–shell TiO_2 hierarchical microspheres (TiO_2 HYSHMs) consisting of small nanoparticles have been fabricated through a facile template-free solvothermal reaction followed by calcination. The obtained samples were characterized by X-ray diffraction, scanning electron microscopy, transmission electron microscopy, nitrogen adsorption/desorption analysis and Fourier transform infrared spectroscopy. It was found that the microspheres have porous shell (~100 nm in thickness) composed of small nanoparticles with an average diameter of 10 nm. The interspace between the yolk and shell is ~150 nm. The BET specific surface area and pore volume of the sample are 151.1 $m^2 g^{-1}$ and 0.23 $cm^3 g^{-1}$, respectively. Ostwald ripening processes are proposed to explain the growth mechanism of the TiO_2 HYSHMs based on a series of time-dependent experiments. As the anode materials for the lithium ion batteries, TiO_2 HYSHMs exhibit a high initial discharge capacity of 267.6 mAh g^{-1} at 0.25 C and retain 191 mAh g^{-1} even after 40 cycles, indicating good electrochemical performance. These good electrochemical performances could be attributed to the short Li-ion and electron pathways, and enough elastic buffer space to accommodate large volume variation of the special yolk–shell hierarchical structure.

1. Introduction

Lithium ion batteries (LIBs) have been considered as one of the most promising power sources for electric vehicles (EVs) and energy storage systems for wind and solar power energy plants since they were first commercialized about twenty years ago [1]. For

* Corresponding author. School of Chemistry and Chemical Engineering, Collaborative Innovation Center of Henan Province for Green Manufacturing of Fine Chemicals, Henan Province, Key Laboratory of Green Chemical Media and Reactions, Ministry of Education, Henan Normal University, Xinxiang 453007, P. R. China. Tel.: +86 373 3325058; fax: +86 373 3328507.
E-mail address: yanglin1819@163.com (L. Yang).

http://dx.doi.org/10.1016/j.jpowsour.2014.03.081
0378-7753/

most of the commercial LIBs, graphite/carbon is used as an anode material. The graphite/carbon electrode, however, suffers from poor safety thus making them unsuitable for large scale application. The safety issues arise from the dendritic deposition of metal lithium on the anode surface at this relatively low lithium insertion potential of conventional graphite/carbon anode (~0.1 V vs Li/Li^+) [2–5]. Furthermore, the formation of a solid electrolyte interface (SEI) on the anode below 1.0 V (vs Li/Li^+) causes undesirable electrolyte decomposition and consumes valuable Li^+ from the cathode irreversibly [6]. It leads to not only the loss of initial capacity, but also the safety concern of SEI [7]. Therefore, in recent years numerous researches are being carried out to develop alternative anode materials with higher lithium insertion potential [2,8–10].

TiO_2 is regarded as a promising anode material for LIBs with outstanding safety due to its high lithium insertion potential (~1.7 V vs Li/Li^+) [11]. Moreover, the TiO_2 is structurally stable during lithium insertion/extraction [12,13], and hence good cycle stability is theoretically possible. Furthermore, TiO_2 is environmentally benign, highly abundant and low-cost material. Despite these advantages, TiO_2 suffers from low electronic conductivity and Li^+ diffusivity [14], which will seriously limit the rate capability and be prohibitive for its wide practical application. The yolk–shell structure, especially with the hierarchical structure composed of nanoparticles, can improve this problem. The nanoparticle subunits are small enough to shorten Li^+ diffusion path. The interstitial space between nanoparticles together with the space between the yolk and the shell make electrolyte penetrate freely. The large specific area increases amount of contact area between the electrolyte and the electrode for Li^+ insertion/extraction [15,16]. The voids between the yolk and the shell can also serve as a buffering space to the volume variation of the electroactive yolk material during lithium insertion and extraction. A yolk–shell microsphere is different from a core–shell one, which possesses the unique structure of a hollow shell and an encapsulated single spherical core, in which there exists an interstitial space between the shell and the core particle, and therefore the core particle can move freely within the hollow shell [17].

The yolk–shell structures have drawn tremendous interest in recent years because of their potential application in energy storage, chemical sensing, drug delivery, medical imaging, artificial cells, and catalysis [18]. Synthesis of yolk–shell structures based on specific approaches, such as solvothermal, bottom–up, soft templating or spray pyrolysis approaches, etc, was already available according to previous reports [15,19–32]. For example, a group of templating methods have been proven very effective and versatile for synthesizing yolk–shell structures. But a facile template-free method is still a challenge. Moreover, because of the structure complexity and the same chemical composition of the yolk and shell parts, it is in general highly difficult to fabricate homogeneous yolk–shell structure. To the best of our knowledge, there are only a few reports on the synthesis of homogeneous yolk–shell TiO_2 through a template-free solvothermal route [27–29]. Moreover, the application of this kind of yolk–shell TiO_2 in LIBs is up to date extremely sparse. For this reason, it is a great opportunity to design and synthesize a TiO_2 anode material of LIBs on the base of yolk–shell structures.

Herein, we report a simple synthesis of homogeneous yolk–shell TiO_2 hierarchical microspheres (TiO_2 HYSHMs) via a facile template-free solvothermal route and subsequent calcination treatment in air. It only uses tetrabutyl titanate (TBT), oxalic acid dihydrate and ethylene glycol as raw materials. Ostwald ripening processes are proposed to explain the growth mechanism of the TiO_2 HYSHMs. By taking advantage of TiO_2 HYSHMs as anode materials for lithium ion batteries, we demonstrated that the as-synthesized TiO_2 HYSHMs possess high electrochemical activity. We also discussed the possible reasons for the advantage and electrochemical features of TiO_2 HYSHMs as lithium storage material.

2. Experimental

2.1. Materials

Tetrabutyl titanate (TBT) was purchased from the Aladdin Industrial Corporation. Oxalic acid dihydrate was purchased from Chemical Reagent Company of Tianjin (China). Ethylene glycol was purchased from Sinopharm Chemical Reagent Company. All other chemicals were used without further purification. Deionized water was also used in our experiment.

2.2. Synthesis of TiO_2 HYSHMs

TiO_2 HYSHMs were synthesized by a solvothermal reaction followed by calcination. In a typical procedure, oxalic acid dihydrate (10 g) was completely dissolved in ethylene glycol (60 mL) under vigorously magnetic stirring. 0.75 mL TBT was then added under stirring. After that, the mixture was stirred vigorously for 30 min and then transferred into a Teflon-lined stain less-steel autoclave with a capacity of 100 mL. The autoclave was heated at 150 °C and maintained for 12 h. After cooling down to room temperature, the white precipitates were centrifuged and washed with deionized water and absolute ethanol several times, then dried at 80 °C for 8 h. As a result, the white precursor was obtained (denoted as precursor). Finally, the white pure TiO_2 HYSHMs powders were produced after annealing the precursor at 400 °C in air for 5 h.

2.3. Structural characterization

The crystal structure was determined using X-ray diffraction (XRD) (Bruker advance-D8 XRD with Cu Kα radiation, $\lambda = 0.154178$ nm, the accelerating voltage was set at 40 kV with a 100 mA flux). Microstructures and morphologies were investigated using scanning electronic microscopy (SEM, JEOL JSM-6390LV) and transmission electron microscope (TEM, JEM-2100). Nitrogen adsorption/desorption isotherms were determined with an ASAP 2020 (Micromeritics Instruments). Surface area determination and pore analysis were performed by using the Brunauer–Emmett–Teller (BET) method and the Barrett–Joyner–Halenda (BJH) method. Fourier transform infrared spectrographs (FTIR) were recorded on a Bio-Rad FTS-40 Fourier transform infrared spectrophotometer in the wavelength range of 4000–400 cm^{-1}. The spectra were collected at 2 cm^{-1} resolution with 128 scans.

2.4. Electrochemical measurements

To prepare the working electrodes, the as-prepared TiO_2 materials were mixed with carbon black (Super P) and polyvinylidene fluoride (PVDF) binder (70:20:10 by weight) in *N*-methylpyrrolidinone (NMP) to form a slurry. The slurry was then coated onto copper foil using doctor blade and dried overnight in a vacuum oven at 120 °C to form the working electrode. Coin-type half cells (2016-type) were assembled in an argon-filled glove box using lithium foil as the counter electrode. The electrolyte was 1 M $LiPF_6$ in a mixture of ethylene carbonate (EC) and dimethyl carbonate (DMC) (1:1 v/v). Galvanostatic charge/discharge tests were performed in the potential range of 1.0–3.0 V at room temperature by using an LAND CT2001A battery-testing instrument. Cyclic voltammetry (CV) measurements were conducted using CHI660D Electrochemical Workstation.

3. Results and discussion

To synthesize TiO_2 HYSHMs, TBT, oxalic acid dihydrate and ethylene glycol were acted as raw materials. The formation mechanism of yolk–shell structure is shown in Fig. 1. In step 1, a complex is generated when mix the raw materials together. In step 2, the solid spheres are formed under solvothermal conditions. In step 3, the interior of the solid spheres are divided into many discrete regions. In step 4, with solvothermal time increasing, the yolk–shell structure precursor consisting of many nanoparticles is obtained by Ostwald ripening. TiO_2 HYSHMs as the final sample can be generated via the subsequent calcination treatment.

The morphology and internal structure of the precursor and the TiO_2 HYSHMs sample are characterized by SEM and TEM. The results show that both the precursor and product are the yolk–shell structure. The SEM images (Fig. 2a and c) show that both the precursor and the TiO_2 HYSHMs are in size ranges of 0.9–1.7 μm. The size has no obvious changes before and after calcinations. The typical broken microspheres of Fig. 2a and c (inset) show they are yolk–shell structure. The yolk–shell structure can be further confirmed by TEM (Fig. 2b and d). The obvious void space between the yolk and shell can be observed, showing that the yolk–shell structures are formed. The high resolution TEM (HRTEM) image (Fig. 2e) can be further utilized to confirm the hierarchical structure of TiO_2 HYSHMs. It shows that the interspace between the yolk and shell is ~150 nm. The shell (~100 nm in thickness) is composed of small nanoparticles as building blocks. The average diameter of the building blocks is about 10 nm (Fig. 2f, labelled by white circles). In addition, there are obvious voids among the small particles, revealing the porous structure of the shell. The phase and crystal structure of the TiO_2 HYSHMs is confirmed with HRTEM observation, as shown in Fig. 2f. The distance between lattice fringes is 0.35 and 0.19 nm, respectively, which can be assigned to (101) and (200) of anatase phase. The selected area electron diffraction (SAED) pattern (inset of Fig. 2f) also confirms the anatase phase of the annealed sample.

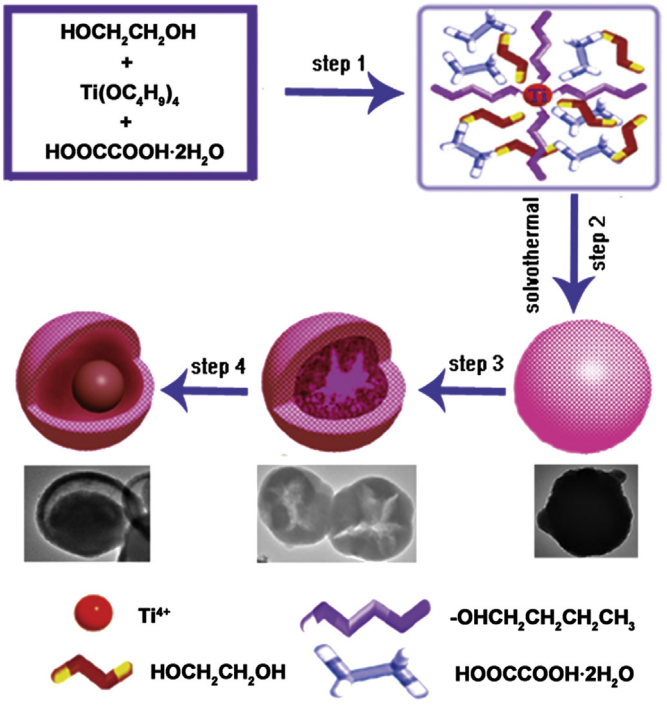

Fig. 1. Schematic illustration of the possible process for the formation of TiO_2 HYSHMs.

The XRD pattern of the precursor by the solvothermal reaction is shown in Fig. 3 (curve a) and the diffraction peaks can be indexed to anatase phase TiO_2 (JCPDS No. 21-1272). The broader and lower intensity of the diffraction peaks indicate the poor TiO_2 crystal nature of the compound. After the precursor calcined at 400 °C, all diffraction peaks (Fig. 3, curve b) are in good agreement with the anatase phase TiO_2 (JCPDS No. 21-1272). The average grain size of the nanocrystals calculated along the (101) plane using the Scherrer formula is about 10 nm for as-prepared TiO_2 HYSHMs, which agrees well with the crystallites size measured from the HRTEM images.

The prepared TiO_2 HYSHMs have large specific surface areas and porous structure. The specific surface areas and porosity of the TiO_2 HYSHMs were investigated by nitrogen adsorption/desorption experiment. The N_2 adsorption/desorption isotherms of the TiO_2 HYSHMs show characteristics of mesoporous materials (Fig. 4a). The Barrett–Joyner–Halenda (BJH) pore size distribution (Fig. 4b) obtained from the isotherm indicates pores ranging from 2 nm to 9 nm. The BET specific surface area and pore volume of the sample are 151.1 $m^2\ g^{-1}$ and 0.23 $cm^3\ g^{-1}$, respectively.

Time-dependent experiments were carried out to shed light on the growth mechanism of the yolk–shell structure. The precursors collected at different time intervals were characterized by TEM method (Fig. 5). It can be seen that the microspheres are formed after solvothermal treatment for 3 h (Fig. 5a). When the reaction time is prolonged to 4 h, the microspheres are retained, but the pristine solid spheres are divided into many discrete regions (Fig. 5b). When the reaction time further increases to 6 h, the yolk–shell structure has formed (Fig. 5c). When the reaction time finally reaches 12 h, the precursor of as-synthesized TiO_2 HYSHMs is obtained (Fig. 2b). Even the reaction time extends to 30 h, the yolk–shell structure can also be remained (Fig. 5d).

XRD patterns (Fig. 6) show that the sample obtained at 3 h reaction time is nearly amorphous. When the reaction time increases to 4 h, the crystal can be observed. The crystallinity of samples becomes better as time increases. The obvious anatase phase TiO_2 can be obtained when the reaction time extends to 30 h, but the crystallinity is still poor.

The FTIR spectra of the prepared TiO_2 HYSHMs and that of the precursors are shown in Fig. 7. For all the samples, the strong absorption bands at ~3417 cm^{-1} and ~1685 cm^{-1} can be observed, which can be attribute to the stretching and bending vibration of the –OH group of absorbed water molecules. The weak absorption band at ~1711 cm^{-1} corresponds to the C=O stretching vibration can be observed from 3 h to 4 h, which could come from oxalic acid dihydrate. When the reaction time is prolonged to 6 h, it becomes very weak. When the reaction time further increases to 12 h, the absorption band disappears. The same changes have also taken place for the CH_2 stretching vibration (1407–1268 cm^{-1}), which originates from the residual carbon species [33] of glycol or butyl. Based on the analysis above, we can conclude that the oxalate and glycol maybe bond with titanium of TBT, resulting the coordination of oxalate/glycol to titanium centers to form complexes $(OOC\text{-}COO)_x Ti(OCH_2CH_2O)_y(OC_4H_9)_z$. During the course of reaction, TiO_2 is produced with the decomposition of the complexes. All peaks of carbon groups disappear in the spectrum of the annealed TiO_2 sample, indicating they have decomposed after calcination. Except for the vibration of –OH, only strong broad peaks in the range of 400–1000 cm^{-1} can be observed from the annealed TiO_2. These peaks are contribution from the anatase phase Ti–O [34], which demonstrates that the pure TiO_2 has been generated, corresponding to the XRD result (curve b in Fig. 3).

Coin-type half cells (2016-type) were fabricated to evaluate the electrochemical properties of the TiO_2 HYSHMs as working electrodes. The cyclic voltammetry (CV) was generated at a scan rate of

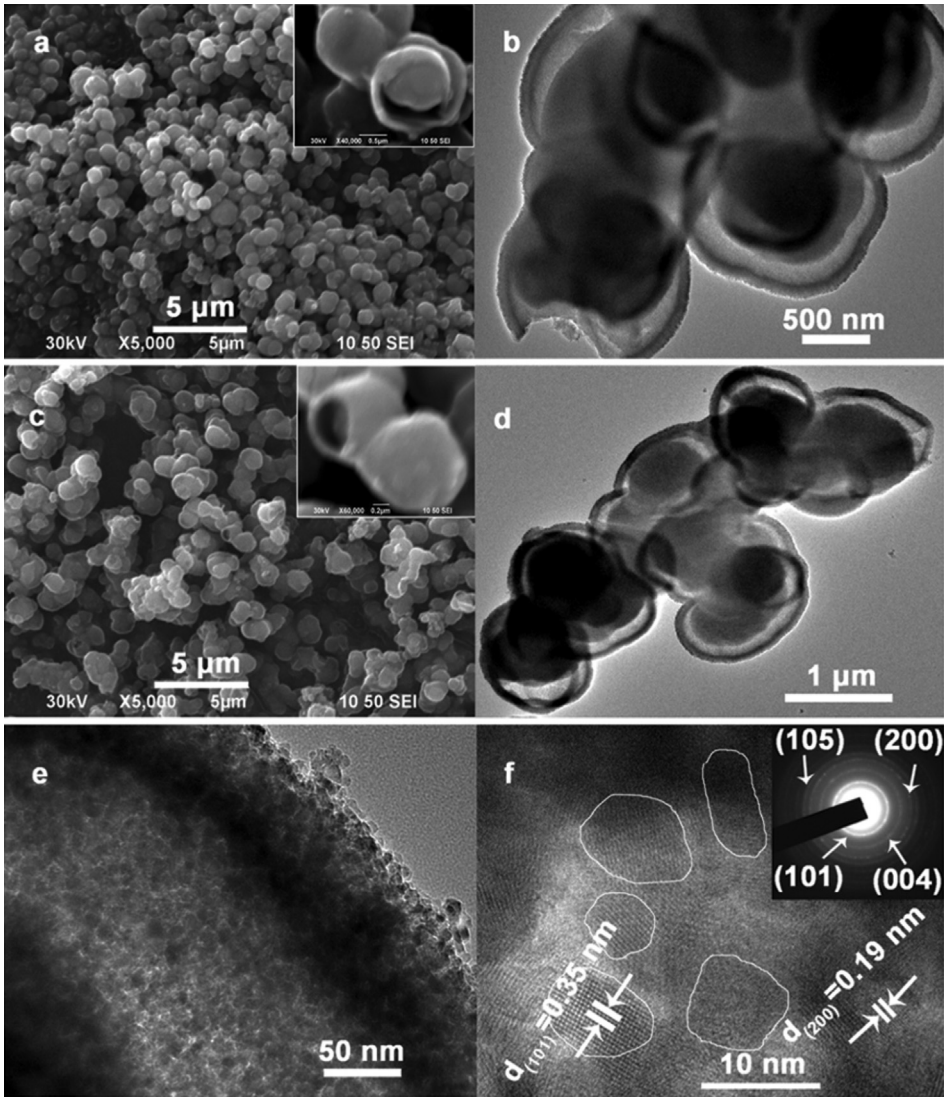

Fig. 2. (a) SEM images of the precursor, the inset is the high-magnification typical broken yolk–shell microsphere; (b) TEM images of the precursor; (c) SEM images of TiO_2 HYSHMs, the inset is the high-magnification typical broken yolk–shell microsphere; (d) TEM image of TiO_2 HYSHMs; (e) HRTEM image of TiO_2 HYSHMs; (f) HRTEM image and SAED pattern (inset) of the TiO_2 HYSHMs (the shell).

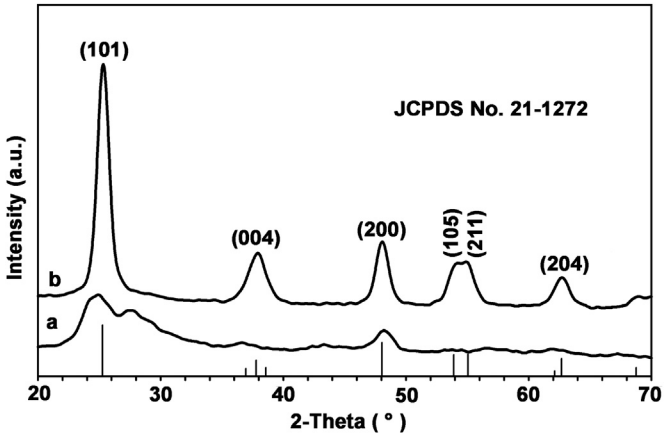

Fig. 3. XRD patterns of the products (a) before and (b) after calcination.

0.1 mV s^{-1} in the potential range from 3.0 to 1.0 V at room temperature (Fig. 8a). The CV curve of the sample exhibits a pair of cathodic/anodic peaks at 1.69 and 2.07 V, which is characteristic for the Li^+ intercalation/deintercalation reaction in anatase TiO_2 [2]. The 0.38 V interval spacing between the cathodic/anodic peaks in this TiO_2 HYSHMs electrode is much lower than that the typical reported in the literature (0.49 V) [35]. Because the peak separation is determined by the overpotential required for the transformation between TiO_2 and Li_xTiO_2, the lower peak potential interval indicates that the lithium inserting reaction of TiO_2 HYSHMs is more easily [36]. The ratio of anodic to cathodic peak currents is nearly 1, which demonstrates that Li^+ intercalates and deintercalates reversibly and this redox system remains in equilibrium throughout the potential scan [35,37].

The charge–discharge voltage profiles of the TiO_2 HYSHMs electrode for the first three cycles at a current rate of 0.25 C (1 C corresponds to 336 mAh g^{-1}) are shown in Fig. 8b. The results are generally consistent with the above CV analysis as well as previously reported data, in which two distinct potential plateaus appear at approximately 1.71 and 1.96 V for discharging and charging

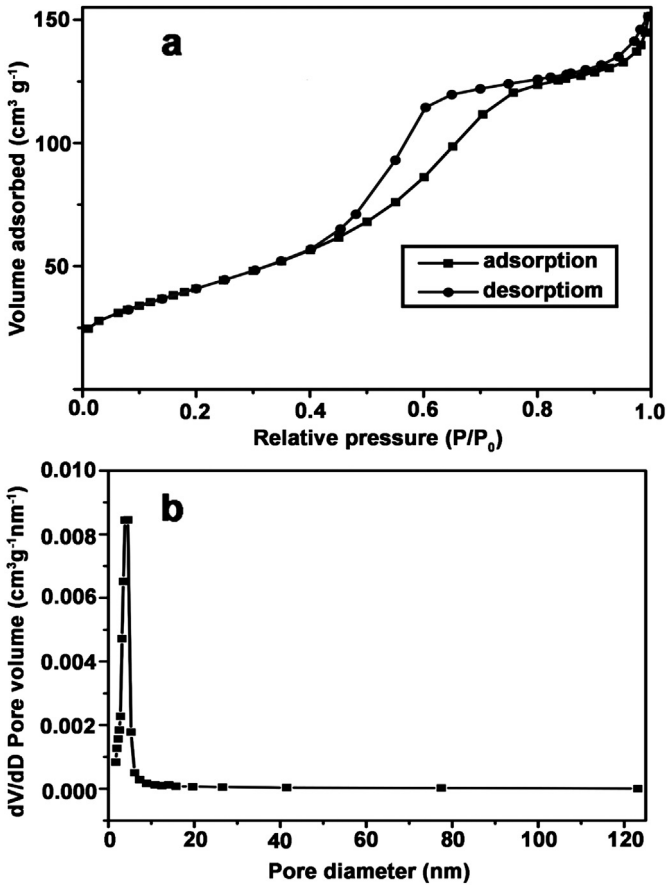

Fig. 4. (a) N_2 adsorption–desorption isotherm of TiO_2 HYSHMs; (b) the pore size distribution calculated from the desorption branch.

processes, corresponding to Li^+ insertion/extraction within the anatase lattice, respectively [38]. The discharge curves can be divided into three different voltage regions, as reported in a previous study [39]. The first stage is fast drop in the potential from the

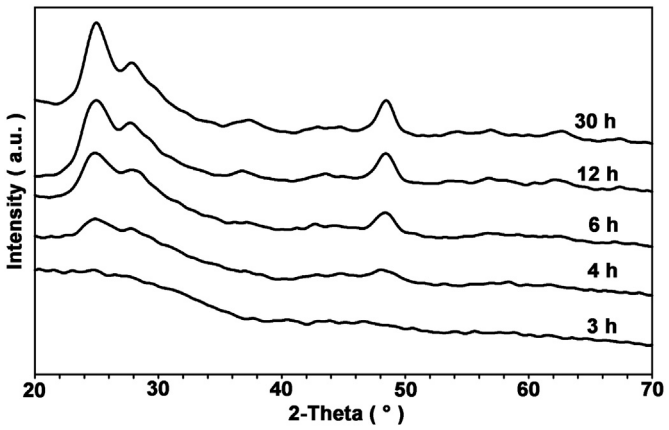

Fig. 6. XRD patterns of solvothermally prepared precursors at different reaction times.

open circuit voltage to a value of ~1.71 V attributed to a solid-solution insertion process. The second stage is the horizontal plateau region, which associated with the process of lithium insertion into the vacant sites of the TiO_2 crystal structure. The last stage is the gradual decay of the voltage between 1.71 and 1.0 V, which is ascribed to further Li^+ insertion into the surface layer of the electrode material. The initial discharge and charge capacities is 267.6 mAh g^{-1} and 231.5 mAh g^{-1}, respectively, leading to an irreversible capacity loss of 13.5%. The initial irreversible capacity loss of other anatase TiO_2 electrodes is usually in the range of 10–30% [8,14,37]. As for the irreversible capacity loss in TiO_2, it is not very well understood and three possible reasons are (i) lithium intercalation into irreversible sites, (ii) side reaction caused by the water absorbed on TiO_2 electrode, and (iii) poor intrinsic electronic conductivity of TiO_2, which have been summarized by literature [8]. Of course, the more accurate reason needs to further study. Coulombic efficiency improve to 95.3% and 98.9% in the 2nd and 3rd cycle, respectively, which confirms the electrode is nearly reversible.

Different rates of charge–discharge were used to investigate the rate performance of the TiO_2 HYSHMs electrode (Fig. 8c). As the

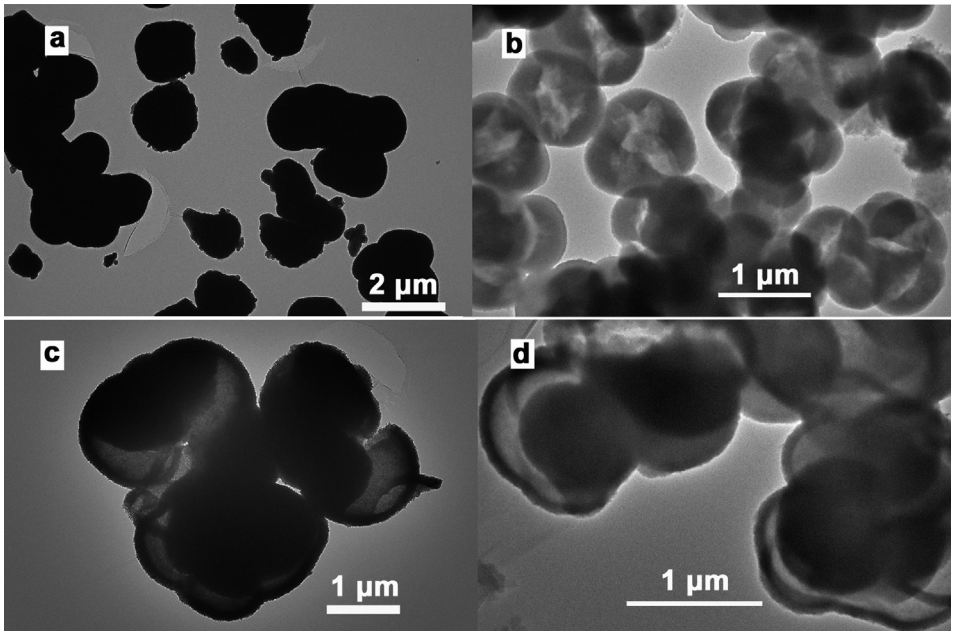

Fig. 5. TEM of solvothermally prepared precursors collected at different reaction times: (a) 3 h, (b) 4 h, (c) 6 h and (d) 30 h, respectively.

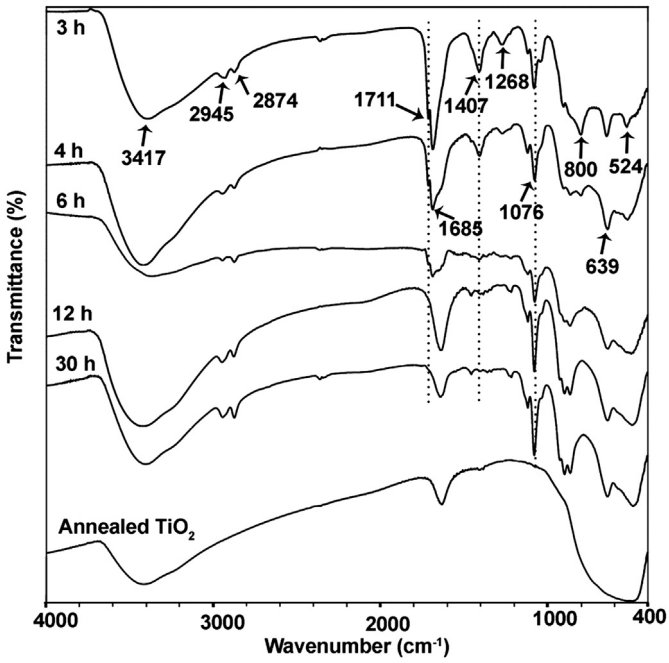

Fig. 7. FTIR spectra of solvothermally prepared precursors at different reaction times and the annealed TiO_2.

charge–discharge rate increases, the discharge capacity decreases from 230.4 mAh g^{-1} (0.5 C) to 198 (1 C), 157.9 (5 C), 127.4 (10 C), and 92.7 (25 C) mAh g^{-1}, respectively. These results show that the TiO_2 HYSHMs exhibit a good rate capability.

In addition, the TiO_2 HYSHMs also exhibit good cyclic performance (Fig. 8d). Cycled at a rate of 0.25 C, a reversible capacity can still be retained as high as 191 mAh g^{-1} after 40 cycles. Cycled at a rate of 0.5 C, the reversible capacity of 142 mAh g^{-1} can still be delivered after 40 cycles. Further increasing the rate to 1, 5, 10 and 25 C, capacities of 132.6, 90.8, 62.3 and 37.09 mAh g^{-1} are obtained after 40 cycles, respectively. In comparison with the reported values of TiO_2-based electrodes, the discharge capacities of the TiO_2 HYSHMs are higher at low rate (0.25 C) and comparable at higher rates [40,41].

The superior electrochemical lithium storage performance is attributed to the unique yolk–shell hierarchical structure. The TiO_2 HYSHMs are composed of porous shells, which are formed by the aggregation of anatase nanocrystals. The diffusion of Li^+ ions is facilitated because the nanocrystal subunits are small enough to shorten Li^+ diffusion path. The unique structure with relatively large surface area endows them with the higher capacity and provides sufficient electrode–electrolyte contact interface. Moreover, the cavity between yolk and shell offers a sufficient void space, which sufficiently alleviates the mechanical stress caused by volume change. Therefore, the electrochemical performance can be enhanced.

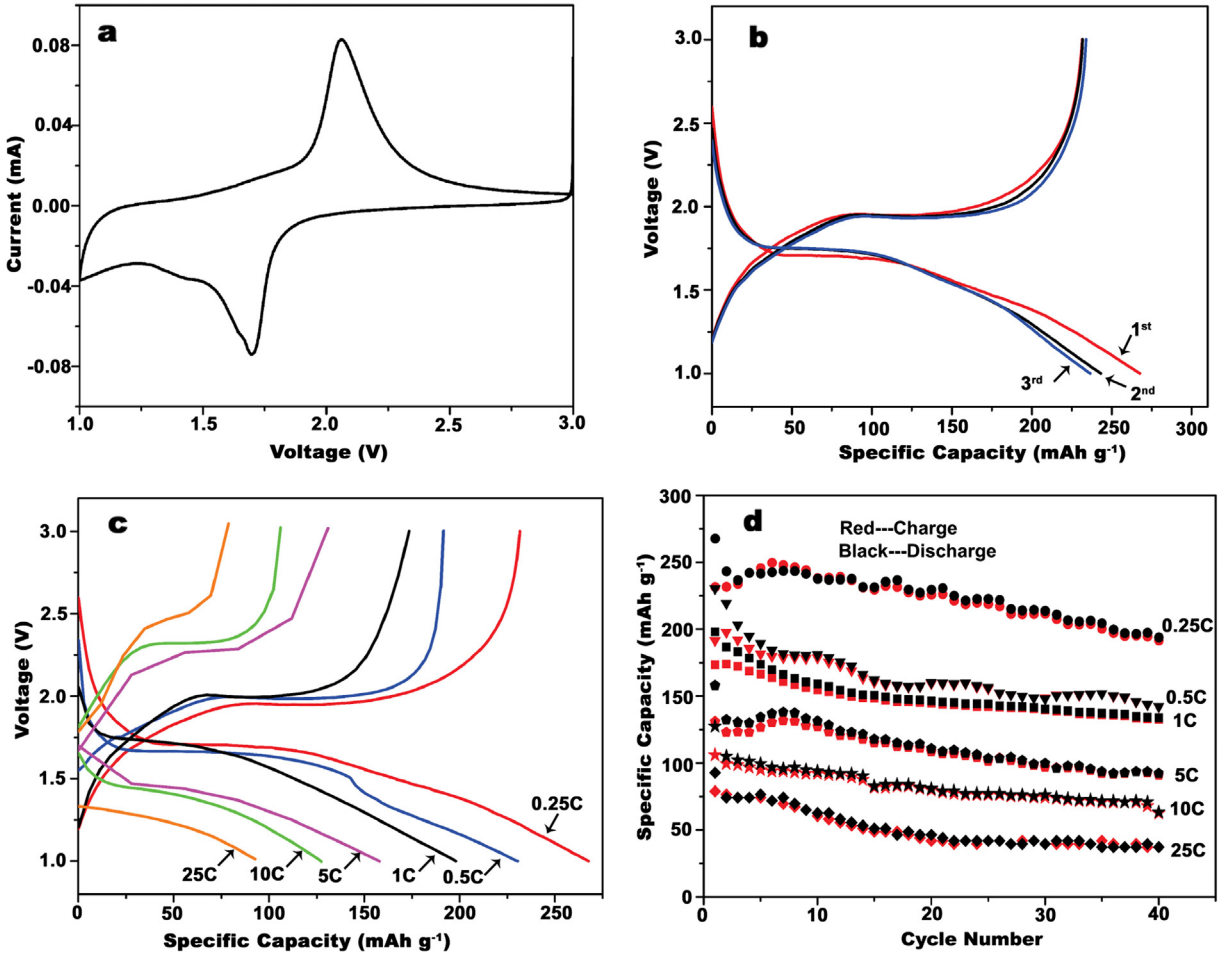

Fig. 8. (a) Cyclic voltammetry of the TiO_2 electrode at a scan rate of 0.1 mV s^{-1} between 1.0 and 3.0 V; (b) charge–discharge profiles at a current rate of 0.25 C for the first, second, and third cycles; (c) charge–discharge profiles of the TiO_2 electrode at different current rates between 0.25 and 25 C; and (d) cycling performance of the TiO_2 electrode at different current rates between 0.25 and 25 C.

4. Conclusions

The TiO_2 HYSHMs consisting of ~10 nm nanoparticles have been fabricated through a facile template-free solvothermal reaction followed by calcination. The diameters of these microspheres range from 0.9 to 1.7 μm. The specific surface area and the pore volume of the microspheres are determined to be 151.1 $m^2 g^{-1}$ and 0.23 $cm^3 g^{-1}$, respectively. The TiO_2 HYSHMs exhibit a high initial discharge capacity of 267.6 mAh g^{-1} at 0.25 C and retain 191 mAh g^{-1} even after 40 cycles, indicating excellent cycling stability. As the charge–discharge rate increases, the discharge capacity decreases from 230.4 mAh g^{-1} (0.5 C) to 198 (1 C), 157.9 (5 C), 127.4 (10 C), and 92.7 (25 C) mAh g^{-1}, respectively. These results show that the TiO_2 HYSHMs exhibit a good rate capability. The enhanced electrochemical performance of the electrode can be attributed to the unique yolk–shell hierarchical structure, which not only facilitates the electrolyte to transport the intercalation and deintercalation of the Li ions, but also accommodates large volume variation during the process of Li ions intercalation. The high performance shows the TiO_2 HYSHMs have a bright prospect when applied in lithium ion batteries.

Acknowledgements

This work was financially supported by the Program for Chang Jiang Scholars and Innovative Research Team in University (Grant No. IRT 1061) and Henan Normal University Innovation Funds for Postgraduate (No. YL201202). We would also like to thank for Engineering Technology Research Center of Motive Power and Key Materials for providing a LAND CT2001A battery-testing instrument.

References

[1] B. Scrosati, J. Garche, J. Power Sources 195 (2010) 2419–2430.
[2] J. Wang, Y.K. Zhou, Y.Y. Hu, R. O'Hayre, Z.P. Shao, J. Phys. Chem. C 115 (2011) 2529–2536.
[3] K.S. Park, A. Benayad, D.J. Kang, S.G. Doo, J. Am. Chem. Soc. 130 (2008) 14930–14931.
[4] J.J. Zhang, Z. Wei, T. Huang, Z.L. Liu, A.S. Yu, J. Mater. Chem. A 1 (2013) 7360–7369.
[5] K. Amine, I. Belharouak, Z.H. Chen, T. Tran, H. Yumoto, N. Ota, S.T. Myung, Y.K. Sun, Adv. Mater. 22 (2010) 3052–3057.
[6] Y. Ma, G. Ji, B. Ding, J.Y. Lee, J. Mater. Chem. 22 (2012) 24380–24385.
[7] J. Liu, G.Z. Cao, Z.G. Yang, D.H. Wang, D. Dubois, X.D. Zhou, G.L. Graff, L.R. Pederson, J.G. Zhang, ChemSusChem 1 (2008) 676–697.
[8] H. Han, T. Song, E.K. Lee, A. Devadoss, Y. Jeon, J. Ha, Y.C. Chung, Y.M. Choi, Y.G. Jung, U. Paik, ACS Nano 6 (2012) 8308–8315.
[9] L.F. Shen, X.G. Zhang, E. Uchaker, C.Z. Yuan, G.Z. Cao, Adv. Energy Mater. 2 (2012) 691–698.
[10] Y.J. Bai, C. Gong, N. Lun, Y.X. Qi, J. Mater. Chem. A 1 (2013) 89–96.
[11] A. Moretti, G.T. Kim, D. Bresser, K. Renger, E. Paillard, R. Marassi, M. Winter, S. Passerini, J. Power Sources 221 (2013) 419–426.
[12] D. Deng, M.G. Kim, J.Y. Lee, J. Cho, Energy Environ. Sci. 2 (2009) 818–837.
[13] S.B. Yang, X.L. Feng, K. Müllen, Adv. Mater. 23 (2011) 3575–3579.
[14] J.Y. Shin, D. Samuelis, J. Maier, Adv. Funct. Mater. 21 (2011) 3464–3472.
[15] H.C. Pang, P. Cheng, H.B. Yang, J.L. Lu, C.X. Guo, G.L. Ning, C.M. Li, Chem. Commun. 49 (2013) 1536–1538.
[16] H.E. Wang, H. Cheng, C.P. Liu, X. Chen, Q.L. Jiang, Z.G. Lu, Y.Y. Chung, W.J. Zhang, J.A. Zapien, L. Martinu, I. Bello, J. Power Sources 196 (2011) 6394–6399.
[17] M.C. Zhang, Y. Lan, D. Wang, R. Yan, S.N. Wang, L. Yang, W.Q. Zhang, Macromolecules 44 (2011) 842–847.
[18] Y.J. Hong, M.Y. Son, B.K. Park, Y.C. Kang, Small 9 (2013) 2224–2227.
[19] Q.S. Xie, J.G. Li, Q. Tian, R.R. Shi, J. Mater. Chem. 22 (2012) 13541–13547.
[20] H.C. Pang, Y.Q. Dong, S.L. Ting, J.L. Lu, C.M. Li, D.H. Kim, P. Chen, Nanoscale 5 (2013) 7790–7794.
[21] M.Y. Son, Y.J. Hong, Y.C. Kang, Chem. Commun. 49 (2013) 5678–5680.
[22] L.N. Jin, Q. Liu, W.Y. Sun, Mater. Lett. 102–103 (2013) 112–115.
[23] C.M. Sim, Y.J. Hong, Y.C. Kang, ChemSusChem 6 (2013) 1320–1325.
[24] S.H. Choi, Y.J. Hong, Y.C. Kang, Nanoscale 5 (2013) 7867–7871.
[25] C.M. Sim, S.H. Choi, Y.C. Kang, Chem. Commun. 49 (2013) 5978–5980.
[26] J.Y. Zhong, C.B. Cao, H. Liu, Y.L. Ding, J. Yang, Ind. Eng. Chem. Res. 52 (2013) 1303–1308.
[27] J.Y. Liao, H.P. Lin, H.Y. Chen, D.B. Kuang, C.Y. Su, J. Mater. Chem. 22 (2012) 1627–1633.
[28] W.Q. Fang, X.H. Yang, H.J. Zhu, Z. Li, H.J. Zhao, X.D. Yao, H.G. Yang, J. Mater. Chem. 22 (2012) 22082–22089.
[29] H. Wang, B.L. Wang, S.Y. Ma, Chin. Chem. Lett. 24 (2013) 260–263.
[30] N. Liu, H. Wu, M.T. McDowell, Y. Yao, C.M. Wang, Y. Cui, Nano Lett. 12 (2012) 3315–3321.
[31] W. Li, Y.H. Deng, Z.X. Wu, X.F. Qian, J.P. Yang, Y. Wang, D. Gu, F. Zhang, B. Tu, D.Y. Zhao, J. Am. Chem. Soc. 133 (2011) 15830–15833.
[32] J. Liu, H.Q. Yang, F. Kleitz, Z.G. Chen, T.Y. Yang, E. Strounina, G.Q. Lu, S.Z. Qiao, Adv. Funct. Mater. 22 (2012) 591–599.
[33] H. Guo, D.X. Tian, L.X. Liu, Y.P. Wang, Y. Guo, X.J. Yang, J. Solid State Chem. 201 (2013) 137–143.
[34] G.Z. Liao, S. Chen, X. Quan, Y.B. Zhang, H.M. Zhao, Appl. Catal. B 102 (2011) 126–131.
[35] Y.M. Jiang, K.X. Wang, X.X. Guo, X. Wei, J.F. Wang, J.S. Chen, J. Power Sources 214 (2012) 298–302.
[36] J.P. Wang, Y. Bai, M.Y. Wu, J. Yin, W.F. Zhang, J. Power Sources 191 (2009) 614–618.
[37] J.Z. Chen, L. Yang, Y.F. Tang, J. Power Sources 195 (2010) 6893–6896.
[38] S.J. Ding, J.S. Chen, Z.Y. Wang, Y.L. Cheah, S. Madhavi, X. Hu, X.W. Lou, J. Mater. Chem. 21 (2011) 1677–1680.
[39] C.H. Jiang, M.D. Wei, Z.M. Qi, T. Kudo, I. Honma, H.S. Zhou, J. Power Sources 166 (2007) 239–243.
[40] M. Samiee, J. Luo, J. Power Sources 245 (2014) 594–598.
[41] J.Y. Shin, J.H. Joo, D. Samuelis, J. Maier, Chem. Mater. 24 (2012) 543–551.